Dalton Transactions

ROYAL SOCIETY OF CHEMISTRY

PAPER

View Article Online
View Journal | View Issue

Cite this: *Dalton Trans.*, 2026, **55**, 3786

$Ba_3BiPbREO(BO_3)_4$ (RE = Pr, Nd, Gd, and Dy): two-dimensional rare-earth antiferromagnets with a geometrically-perfect triangular lattice directed by a triangular BO_3 unit

Yun Lv,[a] Yanhong Wang,[a,d] Nian Shi,[a] Keke Huang,[b] Jinkui Tang[c] and Hongcheng Lu *[a,d]

Received 23rd December 2025,
Accepted 22nd January 2026

DOI: 10.1039/d5dt03066h

rsc.li/dalton

The synthesis of novel two-dimensional (2D) triangular frustrated compounds is important for providing various platforms to investigate exotic quantum magnetism. Here, we successfully synthesised a series of RE-based magnetic compounds $Ba_3BiPbREO(BO_3)_4$ (RE = Pr, Nd, Gd, and Dy) with a geometrically-perfect 2D triangular lattice directed by the triangular BO_3 unit. These compounds stabilise 2D layered structures in the hexagonal ($P6_3/mmc$) crystal system, where magnetic ions are linked by BO_3 to form a perfect triangular frustrated lattice. The magnetisation susceptibility results show that all synthesised compounds $Ba_3BiPbREO(BO_3)_4$ exhibit dominant antiferromagnetic (AFM) interactions, with no long-range order (LRO) down to 2 K, which is further confirmed by specific heat measurements. Additionally, their thermal stability and attenuated total reflectance Fourier-transform infrared (ATR-FTIR) and ultraviolet-visible-near-infrared (UV-Vis-NIR) diffuse reflectance spectra are also reported. This work provides a series of RE-based magnetic compounds with a two-dimensional triangular frustrated lattice, offering novel model materials for further investigation on rare-earth-based frustrated magnetism.

Introduction

Two-dimensional (2D) frustrated antiferromagnets have attracted intense research interest due to their unusual quantum phenomena like quantum spin liquids (QSLs), fractional excitations, relationship to superconductivity, and potential applications in quantum computing.[1–7] Common 2D frustrated systems mainly focus on the triangular lattice, the Kagomé lattice, and the honeycomb lattice.[8–15] Among them, the triangular lattice is the most representative system for predicting the realisation of the two-dimensional quantum spin liquid state.[16–18] Typical examples of two-dimensional transition metal magnetic compounds with a triangular lattice include κ-$(BEDT\text{-}TTF)_2Cu_2(CN)_3$,[19] Cs_2CuBr_4,[20] $Na_2BaCo(PO_4)_2$,[21] $Sr_3NiTa_2O_9$,[22] $NiGa_2S_4$,[23] $Ba_3NiSb_2O_9$,[24] and so on.

In addition to transition-metal-based magnetic frustrated systems, RE-based frustrated materials have also been widely investigated over the past decade due to their strong spin–orbit coupling and the crystal field effects of 4f electrons, which can lead to high magnetic anisotropy and a wide variety of magnetic phenomena.[25,26] So far, several RE-based antiferromagnets with 2D triangular lattices have been studied, such as $YbMgGaO_4$,[27] $REZnAl_{11}O_{19}$ (RE = Pr, Nd, and Sm–Tb),[28] $REMgAl_{11}O_{19}$ (RE = Pr and Nd),[29] $CsRESe_2$ (RE = La–Lu),[30] $Ba_6RE_2Ti_4O_{17}$ (RE = Nd, Sm, Gd, and Dy–Yb),[18] and so on. Meanwhile, novel quantum phenomena have been observed in some of these magnetic compounds. For example, spin glass states exist in $YbZnGaO_4$ [31] and $CsDySe_2$;[30] the Berezinskii–Kosterlitz–Thouless (BKT) phase has been found in $TmMgGaO_4$[32] and so on. However, the chemical synthesis of such magnetic models with specific frustrated lattices is random in experiments. Therefore, it is crucial to rationally design and systematically synthesise more novel rare-earth magnetic compounds with a triangular lattice for exploring their quantum magnetism.

Generally, in order to design and synthesize new magnetic compounds, various basic building units, including VO_4, PO_4, IO_3, SeO_3 and BO_3 groups, have been used to mediate magnetic ions, such as $K_3Yb(VO_4)_2$,[33] $SrMn_2(VO_4)_2{\cdot}(H_2O)_2$,[34] $Rb_3Yb(PO_4)_2$,[35] γ-$Co_2(PO_4)(OH)$,[36] MIO_3F (M = Co and Ni),[37]

[a]*Key Laboratory of Materials Chemistry for Energy Conversion and Storage, School of Chemistry and Chemical Engineering, Hubei Key Laboratory of Materials Chemistry and Service Failure, Huazhong University of Science and Technology, Wuhan, 430074, China. E-mail: HCl@hust.edu.cn*
[b]*State Key Laboratory of Inorganic Synthesis and Preparative Chemistry, College of Chemistry, Jilin University, Changchun 130012, China*
[c]*State Key Laboratory of Rare Earth Resource Utilization, Changchun Institute of Applied Chemistry, Chinese Academy of Sciences, Changchun, 130022, China*
[d]*Wuhan National High Magnetic Field Center, Huazhong University of Science and Technology, Wuhan, 430074, China*

$CaNi_2(SeO_3)_3{\cdot}2H_2O$,[38] $Ba_2M(SeO_3)_2Cl_2$ (M = Cu, Ni, Co, and Mn),[39] $BaCuB_2O_5$,[40] $KBaRE(BO_3)_2$ (RE = Sm, Eu, Gd, Tb, Dy, Ho, Er, Tm, and Yb),[41] and so on. Recently, our group have successfully synthesised transition metal-based magnetic triangular systems $KMB_4O_6F_3$ (M = Co, Fe, and Ni) using the triangular BO_3 group.[42–44] Meanwhile, Xuean Chen and Xiaoyan Song *et al.* reported the interesting luminescence properties of $Ba_3BiPbEuO(BO_3)_4$ [45] and its isostructural compound $Ba_4BiPbTbO(BO_3)_4$.[46] In these structures, RE^{3+} ions are connected by the BO_3 group to form a two-dimensional triangular lattice, making them ideal models for studying frustrated magnetism. In this work, we have successfully synthesised a series of rare earth-based magnetic compounds with the formula $Ba_3BiPbREO(BO_3)_4$ (RE = Pr, Nd, Gd, and Dy) and investigated their magnetic properties. Magnetic susceptibility results show no long-range order (LRO) down to 2 K for all four compounds, which is further confirmed by heat capacity results, probably owing to the spin frustration in the triangular lattice. Additionally, their thermal stability, ATR-FTIR spectra and UV-Vis-NIR diffuse reflectance spectra are also reported.

Experimental

Synthesis

The starting materials of praseodymium oxide (Pr_6O_{11}, 99.9%, Shanghai Aladdin Biochemical Technology Co., Ltd), neodymium oxide (Nd_2O_3, 99.99%, Shanghai Aladdin Biochemical Technology Co., Ltd), dysprosium oxide (Dy_2O_3, 99.99%, Shanghai Aladdin Biochemical Technology Co., Ltd), gadolinium oxide (Gd_2O_3, 99.99%, Shanghai Aladdin Biochemical Technology Co., Ltd), bismuth oxide (Bi_2O_3, 99.99%, Shanghai Aladdin Biochemical Technology Co., Ltd), lead oxide (PbO, 99.97%, Shanghai Aladdin Biochemical Technology Co., Ltd), barium carbonate ($BaCO_3$, 99%, Sinopharm Chemical Reagent Co. Ltd), and boric acid (H_3BO_3, 99.5%, Shanghai Aladdin Biochemical Technology Co., Ltd) were used as received.

Powder samples of $Ba_3BiPbREO(BO_3)_4$ (RE = Pr, Nd, Gd, and Dy) were prepared by a solid-state reaction. The raw materials were mixed thoroughly according to the stoichiometric ratio, pressed into pellets, and preheated in an alumina crucible at 500 °C for 12 h. For $Ba_3BiPbPrO(BO_3)_4$, the product was ground again and pressed into a pellet and then sintered in an alumina crucible at 750 °C for 48 h. For $Ba_3BiPbREO(BO_3)_4$ (RE = Nd, Gd, and Dy), the products need to be sintered at 850 °C for 48 h to obtain the pure-phase powder samples.

Large single crystals of $Ba_3BiPbREO(BO_3)_4$ (RE = Pr and Gd) were grown in a platinum crucible by melting a mixture of $BaCO_3$ (6.0 mmol), Bi_2O_3 (4.2 mmol), PbO (4.2 mmol), Gd_2O_3 (1.2 mmol), Pr_6O_{11} (0.4 mmol), and H_3BO_3 (9.6 mmol). The powder was heated to 800 °C for 48 h, followed by programmed cooling at a rate of 20 °C h^{-1} to room temperature. As shown in Fig. S1, millimetre-sized green transparent crystals of $Ba_3BiPbPrO(BO_3)_4$ and colourless transparent crystals of $Ba_3BiPbGdO(BO_3)_4$ were obtained in the platinum crucible, respectively, and their structures were determined by single-crystal X-ray diffraction. The single crystal samples of the other two compounds are ongoing.

Crystallographic determination

Powder X-ray diffraction data were recorded using a Rigaku SmartLab SE powder X-ray diffractometer with Cu Kα radiation (λ = 1.54184 Å) over a 2θ range of 5–120°. The single-crystal X-ray diffraction experiments for the $Ba_3BiPbREO(BO_3)_4$ compounds (RE = Pr and Gd) were conducted at room temperature using a Rigaku XtaLAB mini II with Mo Kα radiation (λ' = 0.71073 Å) and the data were processed using the CrysAlisPro program. All the reflection intensities were corrected by multi-scan methods, and the structure was solved by intrinsic phasing followed by refinement using full-matrix least-squares techniques with the SHELXL crystallographic program within Olex 2 software.[47] The atomic occupancies of Bi and Pb were refined using the EXYZ and SUMP instructions, and there was occupancy disorder of Bi and Pb, which has also been reported in other compounds such as $Ba_3BiPbEuO(BO_3)_4$,[45] $Pb_3BiV_3O_{12}$,[48] $PbBi_2Nb_2O_9$,[49] and so on. In addition, the O2 and B2 atoms in $Ba_3BiPbPrO(BO_3)_4$ were modelled using the geometric constraint ISOR. The main crystallographic data and structure refinement information of $Ba_3BiPbPrO(BO_3)_4$ and $Ba_3BiPbGdO(BO_3)_4$ are shown in Table 1. The structures of all four compounds $Ba_3BiPbREO(BO_3)_4$ (RE = Pr, Nd, Gd, and Dy) were refined by the Rietveld method based on the crystallographic information files using the FullProf program package.[50] The crystal structure of $Ba_3BiPbGdO(BO_3)_4$ was used as the initial model for Rietveld refinements of $Ba_3BiPbNdO(BO_3)_4$ and $Ba_3BiPbDyO(BO_3)_4$, since single-crystal samples were not obtained. All Rietveld refinement results are listed in Table S1. The crystallographic data of all four com-

Table 1 Crystal data and structure refinements for $Ba_3BiPbPrO(BO_3)_4$ and $Ba_3BiPbGdO(BO_3)_4$

Formula	$Ba_3BiPbPrOB_4O_{12}$	$Ba_3BiPbGdOB_4O_{12}$
Formula weight (g mol^{-1})	1220.34	1236.68
Temperature (K)	298	298
Crystal system	Hexagonal	Hexagonal
Space group	$P6_3/mmc$	$P6_3/mmc$
a (Å)	5.3940(12)	5.4387(4)
b (Å)	5.3940(12)	5.4387(4)
c (Å)	26.940(7)	26.384(2)
α (°)	90	90
β (°)	90	90
γ (°)	120	120
V (Å^3)	678.8(3)	675.88(11)
Z	2	2
Max. θ (°)	24.968	29.970
λ' (Mo Kα) (Å)	0.71073	0.71073
ρ_{calc} (g cm^{-3})	5.970	6.077
μ (mm^{-1})	37.418	38.882
F (000)	1032.0	1042.0
R_{int}	0.0749	0.0553
R_1, wR_2 [$I \geq 2\sigma(I)$][a]	0.0524, 0.1082	0.0587, 0.1291
R_1, wR_2 [all data]	0.0861, 0.1175	0.0745, 0.1376
Goodness-of-fit	1.068	1.140

[a] $R_1 = \sum||F_o| - |F_c||/\sum|F_o|$ and $wR_2 = \{\sum w[(F_o)^2 - (F_c)^2]^2/\sum w[(F_o)^2]^2\}^{1/2}$.

pounds have been deposited into the CCDC database (CCDC 2466013–2466016).

Scanning electron microscopy

The elemental distributions of samples were characterised by energy-dispersive X-ray spectroscopy (EDS-mapping) analyses using a Tescan Mira LMS.

Thermal analysis

The thermogravimetric measurements were performed with a PerkinElmer STA8000 TG analyser using an Al_2O_3 crucible. The samples were heated at a rate of 10 °C min^{-1} under a N_2 atmosphere from ambient temperature to 980 °C.

ATR-FTIR spectra and UV-Vis-NIR diffuse reflectance spectra

The ATR-FTIR spectra were collected using a Bruker Vertex 70 FTIR spectrometer in the range of 400–4000 cm^{-1}. UV-Vis-NIR diffuse reflectance spectra were collected using a Shimadzu UV-3600 spectrophotometer in the diffuse reflectance range of 200–2400 nm.

Magnetic measurements

The magnetic measurements were performed with a Quantum Design MPMS superconducting quantum interference device (SQUID) magnetometer. The temperature-dependent magnetic susceptibility data were collected between 2 and 300 K at 0.1 T. The magnetic-field dependent magnetisation data were collected between −7 and 7 T at 2 K. The magnetic susceptibilities were corrected by subtracting the diamagnetic contribution estimated from Pascal's constants.[51]

Specific heat

The specific heat was measured in the temperature range between 2 K and 30 K at 0 T using a Physical Property Measurement System (PPMS-9 T). The samples were pressed into pellets from the powder samples.

Results and discussion

Structural descriptions

The purity of the isostructural compounds $Ba_3BiPbREO(BO_3)_4$ (RE = Pr, Nd, Gd, and Dy) was confirmed by PXRD patterns, and the crystal structures have been refined by the Rietveld refinement method, as shown in Fig. 1. The $Ba_3BiPbREO(BO_3)_4$ compounds (RE = Pr, Nd, Gd, and Dy) are isostructural; therefore, only the crystal structure of $Ba_3BiPbGdO(BO_3)_4$ is described below. $Ba_3BiPbGdO(BO_3)_4$ crystallizes in the hexagonal space group $P6_3/mmc$ (no. 194) with unit cell parameters of a = 5.4387(4) Å, c = 26.384(2) Å, and Z = 2 (Table 1). The crystal structure of $Ba_3BiPbGdO(BO_3)_4$ consists of two-dimensional $[Gd(BO_3)_2]^{3-}$ layers in the ab plane, which are separated by the cations of Bi^{3+}, Pb^{2+}, and Ba^{2+} and anions of $(BO_3)^{3-}$ and O^{2-} along the c axis (Fig. 2a). The Bi^{3+} and Pb^{2+} cations occupy in the same 4e Wyckoff site. In the $[Gd(BO_3)_2]^{3-}$ layers, the magnetic Gd^{3+} ions are bridged by triangular BO_3 groups

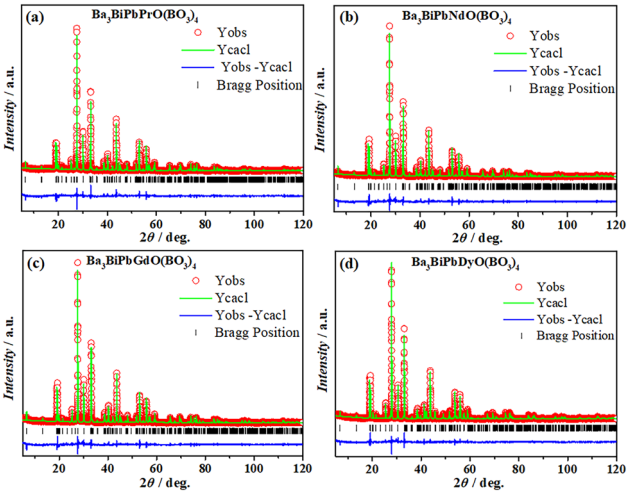

Fig. 1 Rietveld refinement results of $Ba_3BiPbREO(BO_3)_4$. (a) $Ba_3BiPbPrO(BO_3)_4$; (b) $Ba_3BiPbNdO(BO_3)_4$; (c) $Ba_3BiPbGdO(BO_3)_4$; and (d) $Ba_3BiPbDyO(BO_3)_4$.

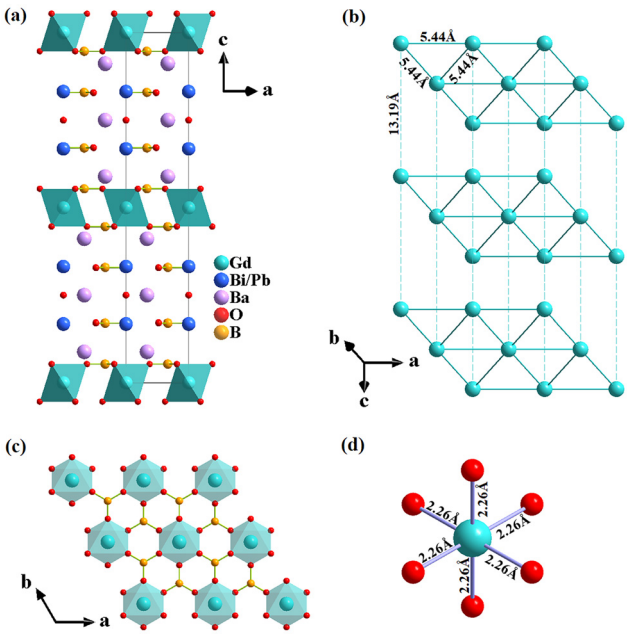

Fig. 2 Crystal structure of $Ba_3BiPbGdO(BO_3)_4$. (a) View along the b axis; (b) the stacking of the Gd^{3+} triangular lattice along the c axis; (c) the $[Gd(BO_3)_2]^{3-}$ triangular lattice in the ab plane; and (d) local coordination environment of the magnetic Gd^{3+} ion.

and form a triangular lattice of Gd^{3+}, as shown in Fig. 2b and c. The shortest intralayer Gd···Gd distance in the triangular lattice is 5.4387(3) Å, while the shortest interlayer Gd···Gd distance is 13.192(1) Å. Each magnetic Gd^{3+} cation is equally coordinated by six O^{2-} ions from the triangular BO_3 groups and forms a GdO_6 octahedron with Gd–O bond lengths of 2.265 (12) Å (Fig. 2d). The EDS mapping results (Fig. S2) indicate the compounds only contain the constituent elements of Ba, Bi, Pb, RE, B and O with uniform distributions. It is worth noting

that, due to the low atomic numbers and low energy, boron atoms cannot be accurately measured, as reported in $Ba_4BiTbO(BO_3)_4$ [46] and other borates.[52,53]

Thermal analysis

Fig. 3 shows the TG curves of $Ba_3BiPbREO(BO_3)_4$ (RE = Pr, Nd, Gd, and Dy). $Ba_3BiPbPrO(BO_3)_4$ exhibits good thermal stability up to 850 °C and then begins to decompose. Interestingly, for $Ba_3BiPbREO(BO_3)_4$ (RE = Nd, Gd, Dy), there is no significant weight loss up to 900 °C, indicating their excellent thermal stability.

ATR-FTIR spectra

The isostructural compounds $Ba_3BiPbREO(BO_3)_4$ (RE = Pr, Nd, Gd, and Dy) show similar infrared spectra in the range of 400–4000 cm^{-1} (Fig. S3). Generally, all the absorption peaks in the range of 500–1400 cm^{-1} are due to the planar triangular BO_3 group. The peaks at 566 cm^{-1}, 596 cm^{-1} and 648 cm^{-1} can be assigned to the in-plane bending of B–O (ν_4), the peaks at 716 cm^{-1} and 772 cm^{-1} arise due to the out-of-plane bending of B–O (ν_2), the weak peaks at 899 cm^{-1} and 955 cm^{-1} are attributed to the symmetric stretching of B–O (ν_1), and the obvious broad absorption peaks at 1148 cm^{-1}, 1208 cm^{-1} and 1264 cm^{-1} originate from the B–O asymmetric stretching (ν_3) of the BO_3 group,[42,54–56] as shown in Fig. 4.

UV-Vis-NIR diffuse reflectance spectra

The UV-Vis-NIR spectra of $Ba_3BiPbREO(BO_3)_4$ (RE = Pr, Nd, Gd, and Dy) are shown in Fig. 5. For $Ba_3BiPbPrO(BO_3)_4$, the electronic transition from the $4f^2$ configuration in the $^3H_4$ ground state leads to distinct absorption bands in the visible range of the UV spectrum, at 442–480 nm and 590 nm, corresponding to transitions from $^3H_4$ to $^3P_{0,1,2}$ and $^1D_2$.[57,58] This is in good agreement with the green colour of the sample. Meanwhile, three absorption bands in the near-infrared region, at 1402 nm, 1482 nm, and 1835 nm, correspond to transitions from $^3H_4$ to $^3F_{4,3,2}$.[59,60] In the UV spectrum of $Ba_3BiPbNdO(BO_3)_4$, six absorption bands are observed at 528 nm, 587 nm, 682 nm, 745 nm, 806 nm, and 879 nm,

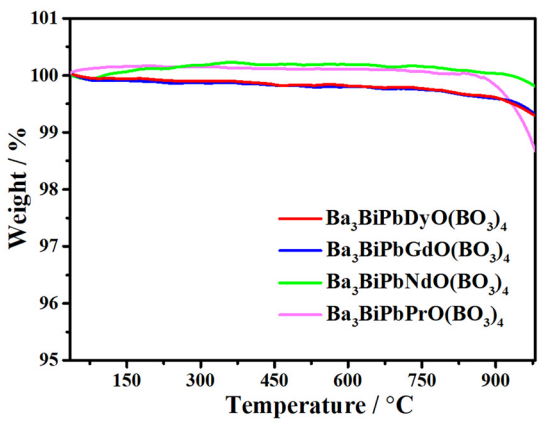

Fig. 3 TGA curves of $Ba_3BiPbREO(BO_3)_4$ (RE = Pr, Nd, Gd, and Dy).

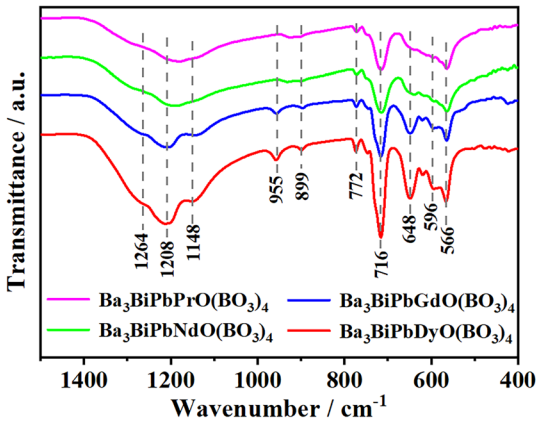

Fig. 4 FTIR spectra of $Ba_3BiPbREO(BO_3)_4$ (RE = Pr, Nd, Gd, and Dy) in the range of 400–1500 cm^{-1}.

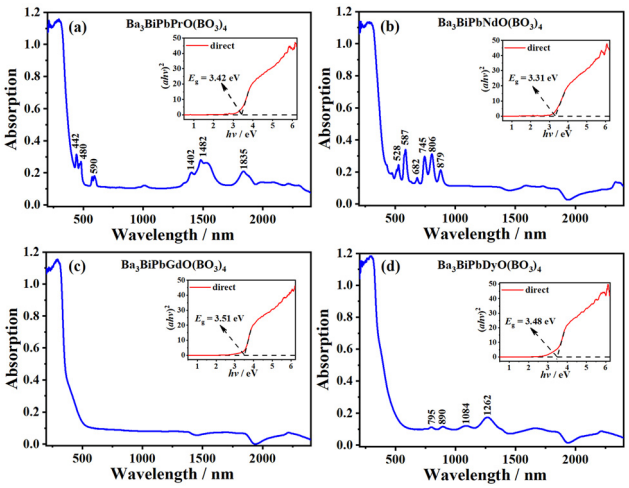

Fig. 5 UV-Vis-NIR spectra of (a) $Ba_3BiPbPrO(BO_3)_4$; (b) $Ba_3BiPbNdO(BO_3)_4$; (c) $Ba_3BiPbGdO(BO_3)_4$; and (d) $Ba_3BiPbDyO(BO_3)_4$. The insets show the direct band gap of $Ba_3BiPbREO(BO_3)_4$ (RE = Pr, Nd, Gd, and Dy).

corresponding to the transitions of Nd^{3+} 4f electrons from the ground state $^4I_{9/2}$ to other excited states $^2K_{13/2}$ + $^4G_{9/2}$ + $^4G_{7/2}$, $^4G5/_2$ + $^4G_{7/2}$, $^4F_{9/2}$, $^4F_{7/2}$ + $^4S_{3/2}$, $^4F_{5/2}$ + $^2H_{9/2}$, and $^4F_{3/2}$.[58,61,62] For $Ba_3BiPbGdO(BO_3)_4$, no significant absorption bands were observed in the 200–2400 nm region; therefore, the crystal is colourless. However, the UV spectrum of $Ba_3BiPbDyO(BO_3)_4$ shows four absorption bands observed at 795 nm, 890 nm, 1084 nm, and 1262 nm, which can be attributed to the transitions occurring between specific energy levels, namely the transitions from $^6H_{15/2}$ to $^6F_{5/2}$, $^6F_{7/2}$, $^6F_{9/2}$ + $^6H_{7/2}$, and $^6F_{11/2}$ + $^6H_{9/2}$,[63,64] respectively.

In addition, the optical band gap was calculated using Tauc's formula[65,66] $\alpha h\nu = A(h\nu - E_g)^n$, where h is Planck's constant, ν is the frequency of light, A is a proportional constant, E_g is the band gap, and n denotes the type of optical transition (n = 2 and 1/2 correspond to indirect and direct band gap

transitions). Here, the coefficient α was replaced with the absorbance obtained from the UV-visible spectra, and the $(\alpha h\nu)^{1/n} - h\nu$ relationship was plotted.[46,57] As shown in the inset of Fig. 5 and Fig. S4, the results indicate that the $Ba_3BiPbREO(BO_3)_4$ compounds (RE = Pr, Nd, Gd, and Dy) show direct band gaps with values of 3.42 eV, 3.31 eV, 3.51 eV, and 3.48 eV, respectively.

Magnetic properties

$Ba_3BiPbPrO(BO_3)_4$. The magnetic susceptibility of $Ba_3BiPbPrO(BO_3)_4$ measured at 0.1 T is shown in Fig. 6a. The $\chi(T)$ curve increases upon cooling and no anomaly is observed, indicating that no magnetic LRO occurred down to 2 K. No divergence between the zero-field cooling (ZFC) and field cooling (FC) curves rules out the possibility of spin glass and spin canting behaviours. The Curie–Weiss fitting is performed in the high-temperature range of 200–300 K, leading to an effective magnetic moment $\mu_{eff(HT,Pr)}$ of $3.99(1)\mu_B$ and a Weiss temperature $\theta_{(HT,Pr)}$ of −90.94(9) K (Fig. 6b and Table 2). The effective magnetic moment $\mu_{eff(HT,Pr)}$ value is close to the expected theoretical value of $3.58\mu_B$ for free Pr^{3+} ions. The slope of the $\chi^{-1}(T)$ curve changed below 5 K, suggesting changes in the magnetic moment and spin–spin interactions in the low-temperature region, which are related to the crystal electric field (CEF) effects.[28,67] In the low-temperature range of 2–3 K below the temperature region, the Curie–Weiss fitting gives an effective magnetic moment $\mu_{eff(LT,Pr)}$ of $1.88(3)\mu_B$ and a Weiss temperature $\theta_{(LT,Pr)}$ of −15.76(37) K. The θ value at low temperatures is considerably larger than those reported for $PrMgAl_{11}O_{19}$ (θ = −6.4 K)[25] and $PrZnAl_{11}O_{19}$ (θ = −9.9 K)[26] with a triangular lattice, as well as that for $Pr_2Be_2GeO_7$ (θ = −3.6 K)[12] with a Shastry–Sutherland lattice. This may be interesting for further investigation, particularly in a large single-crystal sample. The negative Weiss temperature reveals the dominant antiferromagnetic (AFM) interactions between the spins of magnetic Pr^{3+} ions. The $\chi T(T)$ value at room temperature is 1.53 emu K mol^{-1} and then decreases upon cooling, further confirming the dominant AFM exchange interactions.

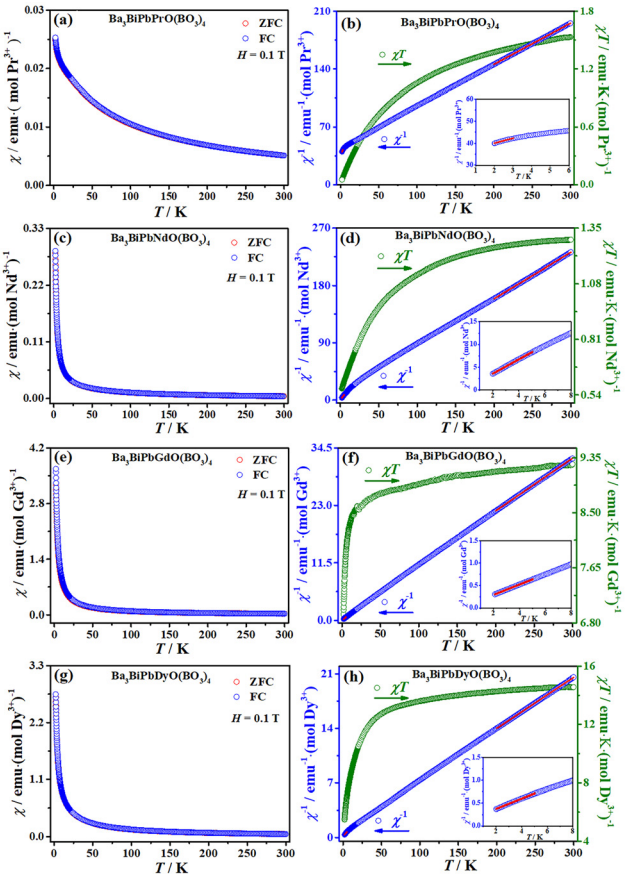

Fig. 6 Magnetic susceptibilities of $Ba_3BiPbREO(BO_3)_4$ (RE = Pr, Nd, Gd, and Dy) measured at 0.1 T. (a, c, e and g) ZFC (red) and FC (blue); (b, d, f) and h) χ^{-1} (blue) and χT (green) of $Ba_3BiPbREO(BO_3)_4$ (RE = Pr, Nd, Gd, and Dy). The red line of χ^{-1} shows Curie–Weiss fitting. The insets of (b), (d), (f) and (h) show χ^{-1} in the low-temperature region.

$Ba_3BiPbNdO(BO_3)_4$. As displayed in Fig. 6c, the $\chi(T)$ curve for $Ba_3BiPbNdO(BO_3)_4$ increases upon cooling and no anomaly is observed, indicating that no magnetic LRO occurred down to 2 K. Similarly, there is no divergence between the ZFC and FC curves, suggesting that the possibility of a spin glass state and spin canting behaviour is ruled out. In the high-temperature region between 200 and 300 K, the Curie–Weiss fitting is applied, yielding an effective magnetic moment $\mu_{(HT,Nd)}$ of 3.32 $(1)\mu_B$ and a Weiss temperature $\theta_{(HT,Nd)}$ of −19.39(16) K, as shown in Fig. 6d and Table 2. The effective magnetic moment $\mu_{(HT,Nd)}$ value is close to the expected theoretical value of $3.62\mu_B$ for free Nd^{3+} ions. In the low-temperature range of 2–5 K, the Curie–Weiss fitting gives an effective magnetic

The magnetic-field-dependent magnetisation for $Ba_3BiPbPrO(BO_3)_4$ is measured at 2 K, as shown in Fig. 7a. The $M(H)$ curve linearly increases with increasing magnetic field up to 7 T, confirming the antiferromagnetic ground state. The magnetisation value at 7 T is $0.24\mu_B$, which is relatively small and far from full saturation.

Table 2 The spin number (S), total angular momentum (J), effective magnetic moments (μ_{eff}) and Curie–Weiss temperatures (θ) of $Ba_3BiPbREO(BO_3)_4$ (RE = Pr, Nd, Gd, and Dy). These fittings were performed in high-temperature (HT) and low-temperature (LT) regions

RE	S	J	μ_J/μ_B	HT fit	θ/K	μ_{eff}/μ_B	LT fit	θ/K	μ_{eff}/μ_B
Pr	1	4	3.58	200–300 K	−90.94(9)	3.99(1)	2–3 K	−15.76(37)	1.88(3)
Nd	3/2	9/2	3.62	200–300 K	−19.39(16)	3.32(1)	2–5 K	−0.24(1)	2.25(1)
Gd	7/2	7/2	7.94	200–300 K	−7.75(14)	8.71(1)	2–5 K	−0.56(1)	8.36(1)
Dy	5/2	15/2	10.65	200–300 K	−13.60(19)	11.04(1)	2–5 K	−1.30(2)	8.41(2)

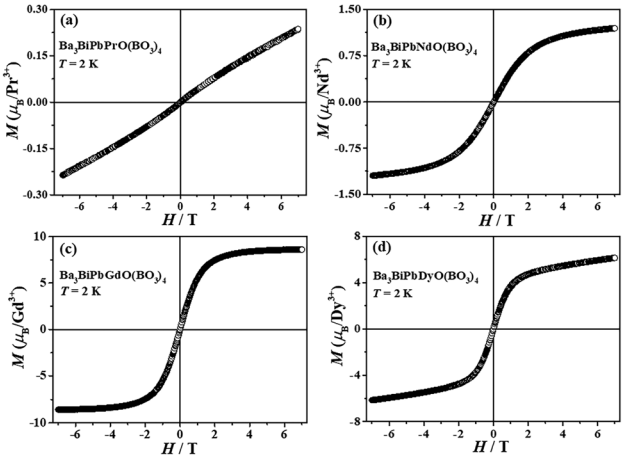

Fig. 7 Field-dependent magnetisations measured at 2 K between −7 T and 7 T for (a) $Ba_3BiPbPrO(BO_3)_4$; (b) $Ba_3BiPbNdO(BO_3)_4$; (c) $Ba_3BiPbGdO(BO_3)_4$; and (d) $Ba_3BiPbDyO(BO_3)_4$.

moment $\mu_{(LT,Nd)}$ of 2.25(1)μ_B and a Weiss temperature $\theta_{(LT,Nd)}$ of −0.24(1) K. The magnetic moment is smaller than that of a free Nd^{3+} ion due to the influence of the CEF effect, which causes more electrons to occupy the lowest-lying Kramers doublet states at lower temperatures. Similar observations have been reported in other frustrated Nd^{3+} compounds, such as $Ba_6Nd_2Ti_4O_{17}$,[18] $Nd_3Sb_3Zn_2O_{14}$,[6] and so on. The negative Weiss temperature indicates that the dominant magnetic exchange interaction in $Ba_3BiPbNdO(BO_3)_4$ is AFM. The value of $\chi T(T)$ at room temperature is 1.29 emu K mol^{-1}, and then gradually decreases upon cooling, further confirming the dominant AFM exchange interactions.

Fig. 7b shows the magnetic-field-dependent magnetisation measured at 2 K for $Ba_3BiPbNdO(BO_3)_4$. At the beginning, the $M(H)$ curve linearly increases below 3 T with a magnetisation of $M_{3\ T}$ = 0.97μ_B, and then increases slowly with the trend to be saturated. The experimental magnetisation of 1.20μ_B at 7 T is close to half of the saturated magnetisation, which is a typical characteristic of powder averaging of Ising spins as observed in other Nd^{3+} systems.[12,28,68]

$Ba_3BiPbGdO(BO_3)_4$. As shown in Fig. 6e, the $\chi(T)$ curve of $Ba_3BiPbGdO(BO_3)_4$ increases upon cooling and no anomaly is observed, indicating that no magnetic LRO occurred down to 2 K. No divergence between the ZFC and FC curves is observed, ruling out the possibility of a spin glass state and spin canting behaviour. The Curie–Weiss fitting is performed in the high-temperature range of 200–300 K, leading to an effective magnetic moment $\mu_{(HT,Gd)}$ of 8.71(1)μ_B and a Weiss temperature $\theta_{(HT,Gd)}$ of −7.75(14) K (Fig. 6f and Table 2). In the low-temperature range between 2 K and 5 K, the Curie–Weiss fitting gives an effective magnetic moment $\mu_{(LT,Gd)}$ of 8.36(1)μ_B and a Weiss temperature $\theta_{(LT,Gd)}$ of −0.56(1) K. The negative Weiss temperature indicates that the dominant magnetic exchange interactions in $Ba_3BiPbGdO(BO_3)_4$ are AFM. The $\chi T(T)$ value at room temperature is 9.25 emu K mol^{-1} and then decreases upon cooling, further confirming the dominant antiferromagnetic exchange interactions.

The magnetic-field-dependent magnetisation for $Ba_3BiPbGdO(BO_3)_4$ is measured at 2 K, as shown in Fig. 7c. At the beginning, the $M(H)$ curve linearly increases below 2 T, confirming the AFM ground state. Then it tends to be saturated at 7 T with a magnetisation value of 8.60μ_B, which is larger than the theoretical saturated magnetisation of Gd^{3+}. Similar phenomena have been reported in other Gd-based compounds Gd_3BWO_9,[69] $RbBaGd(BO_3)_2$,[70] and $GdZnAl_{11}O_{19}$.[28] The underlying mechanism requires further investigation in the future using other techniques, particularly for a large single-crystal sample.

$Ba_3BiPbDyO(BO_3)_4$. The magnetic susceptibility of $Ba_3BiPbDyO(BO_3)_4$ is measured at 0.1 T, as shown in Fig. 6g. The $\chi(T)$ curve increases with no anomaly when decreasing the temperature down to 2 K, suggesting no magnetic LRO for $Ba_3BiPbDyO(BO_3)_4$. There is no divergence between the ZFC and FC curves, suggesting no spin glass state and spin canting behaviour. The Curie–Weiss fitting performed between 200 K and 300 K gives an effective magnetic moment $\mu_{(HT,Dy)}$ of 11.04(1)μ_B and a Weiss temperature $\theta_{(HT,Dy)}$ of −13.60(19) K (Fig. 6h and Table 2). The effective magnetic moment $\mu_{(HT,Dy)}$ value is close to the expected theoretical value of 10.65μ_B for free Dy^{3+} ions. The slope of χ^{-1} varies below 5 K due to CEF effects.[17,71] In the low-temperature range, the Curie–Weiss fitting performed between 2 and 5 K gives an effective magnetic moment $\mu_{(LT,Dy)}$ of 8.41(2)μ_B and a Weiss temperature $\theta_{(LT,Dy)}$ of −1.30(2) K. The negative Weiss temperature indicates that the dominant magnetic exchange interactions in $Ba_3BiPbDyO(BO_3)_4$ are also AFM. The $\chi T(T)$ value at room temperature is 14.56 emu K mol^{-1} and then decreases upon cooling, which further confirms the dominant antiferromagnetic exchange interactions.

The magnetic-field-dependent magnetisation for $Ba_3BiPbDyO(BO_3)_4$ is measured at 2 K, as shown in Fig. 7d. At the beginning, the $M(H)$ curve linearly increases below 1.5 T and then gradually tends to saturation. The magnetisation value at 7 T is 6.14μ_B, which is slightly larger than half of the fully polarised Dy^{3+} moments of 10μ_B due to powder averaging of Ising spins, as reported in $Dy_2Be_2GeO_7$,[12] $Dy_2O_2CN_2$,[68] Dy_3BWO_9,[69] and $RbBaDy(BO_3)_2$.[70]

To better investigate the two-dimensional magnetism of the $Ba_3BiPbREO(BO_3)_4$ compounds, we evaluated the magnitudes of superexchange magnetic interactions and intra/inter-layer dipolar interactions. Here, to evaluate the energy scale of magnetic interactions, the strengths of superexchange interaction (J_{nn}) between local RE^{3+} moments are estimated by the mean field approximation using $J_{nn} = 3\theta/[zS(S+1)]$,[18,72,73] where S denominates the total spin number (for rare earth, S is represented by the total angular momentum J), z is the number of nearest-neighbor spins (z = 6), and θ is the Weiss temperature from low-temperature fitting. Considering the significant spin–orbit coupling, varying crystal electric field (CEF) effects and spin types of RE^{3+}, the quantum number $J = |L \pm S|$ and effective spin S_{eff} = 1/2 were adopted for estimating the nearest-neighbour exchange J_{nn}. For $Ba_3BiPbREO(BO_3)_4$ (RE =

Table 3 The estimated superexchange interaction (J_{nn}), intralayer dipole–dipole interactions (D_{intra}) and interlayer dipole–dipole interactions (D_{inter}) for $Ba_3BiPbREO(BO_3)_4$ (RE = Pr, Nd, Gd, and Dy)

	D (K)		J_{nn} (K)	
RE	D_{intra}	D_{inter}	Using J	Using J_{eff} = 1/2
Pr	0.0140(5)	0.00090(3)	−0.39(1)	—
Nd	0.0200(2)	0.00130(1)	−0.0048(2)	−0.16(1)
Gd	0.2706(8)	0.01892(5)	−0.0178(3)	—
Dy	0.2736(8)	0.01920(5)	−0.0102(2)	−0.87(2)

Nd, Dy), S_{eff} = 1/2 is particularly appropriate because electrons occupy the low-lying Kramers doublet at low temperatures. The dipolar interactions D are calculated using $D = \mu_0\mu_{eff}^2/[4\pi(R_{nn})3k_B]$,[18,68,72,73] where R_{nn} represents intra-layer and inter-layer nearest-neighbour RE–RE distances (D_{intra} and D_{inter}) and μ_{eff} is the effective moment from low-temperature fitting. The calculated superexchange interaction and dipolar interactions are listed in Table 3. Evidently, the intra-layer dipolar interactions (D_{intra}) are approximately 15 times larger than the inter-layer counterpart (D_{inter}). Structurally, superexchange *via* the intra-layer RE–O–B–O–RE path significantly exceeds that *via* the inter-layer RE–O–Bi/Pb–O–Bi/Pb–O–RE path. All estimated interactions indicate that $Ba_3BiPbREO(BO_3)_4$ realizes quasi-two-dimensional magnetism.

Heat capacity

To confirm no occurrence of LRO in $Ba_3BiPbREO(BO_3)_4$ (RE = Pr, Nd, Gd, and Dy), especially at low temperature, the heat capacity measurements were performed from 30 K down to 2 K (Fig. 8). The $C_p(T)$ curve decreases upon cooling and no sharp peak is observed down to 2 K, indicating that no LRO occurred for $Ba_3BiPbREO(BO_3)_4$ (RE = Pr, Nd, Gd, and Dy). These are in good agreement with the magnetic susceptibility results. The slight increases below 5 K (Fig. S5) for $Ba_3BiPbGdO(BO_3)_4$ and $Ba_3BiPbDyO(BO_3)_4$ should be Schottky anomalies, despite that LRO below 2 K cannot be ruled out at this moment. Further investigations using other techniques, such as specific heat and neutron scattering measurements below 2 K, will be performed by collaborating with physicists later, particularly for the large single crystal sample.

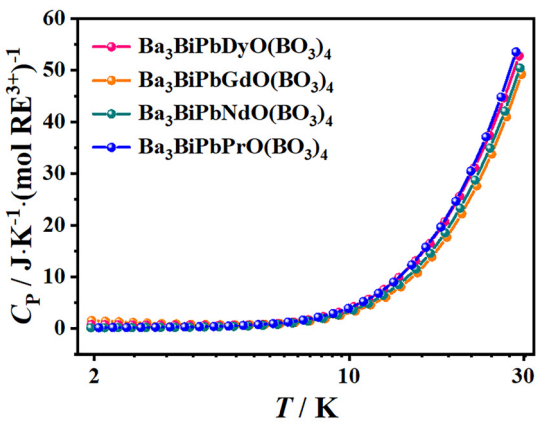

Fig. 8 Specific heat for $Ba_3BiPbREO(BO_3)_4$ (RE = Pr, Nd, Gd, and Dy).

Conclusions

In conclusion, a series of isostructural rare-earth-based magnetic compounds $Ba_3BiPbREO(BO_3)_4$ (RE = Pr, Nd, Gd, and Dy) with a geometrically-perfect triangular magnetic lattice have been successfully synthesised. The magnetisation susceptibility results indicate that dominant interactions between RE^{3+} moments are antiferromagnetic in all four compounds and exhibit no LRO down to 2 K, as further confirmed by specific heat measurements. These RE-based magnetic compounds with a two-dimensional triangular frustrated structure provide a platform for exploring more physical phenomena in rare-earth-based spin-frustrated materials.

Author contributions

Yun Lv: synthesis of samples, formal analysis, data curation, and writing – original draft. Yanhong Wang: writing – review & editing and formal analysis. Nian Shi: data curation and formal analysis. Keke Huang: writing – review & editing and funding acquisition. Jinkui Tang: writing – review & editing and funding acquisition. Hongcheng Lu: writing – review & editing, supervision, resources, funding acquisition, and conceptualization.

Conflicts of interest

There are no conflicts to declare.

Data availability

All experimental procedures and associated data are included in the article and its supplementary information (SI). Supplementary information is available. See DOI: https://doi.org/10.1039/d5dt03066h.

Other data are available upon request from the corresponding author.

CCDC 2466013–2466016 for $Ba_3BiPbREO(BO_3)_4$ (RE = Pr, Nd, Gd, and Dy) contain the supplementary crystallographic data for this paper.[74a–d]

Acknowledgements

This work was supported by the National Natural Science Foundation of China (NSFC No. 22271107 and 22422111), the National Key Research and Development Program (No. 2023YFA1406500), and the Open Funds of the State Key Laboratory of Rare Earth Resource Utilization (RERU2023011).

References

1 L. Balents, *Nature*, 2010, **464**, 199–208.
2 M. Hering, H. Yan and J. Reuther, *Phys. Rev. B: Condens. Matter Mater. Phys.*, 2021, **104**, 064406.
3 C. Broholm, R. J. Cava, S. A. Kivelson, D. G. Nocera, M. R. Norman and T. Senthil, *Science*, 2020, **367**, eaay0668.
4 D. E. Freedman, R. Chisnell, T. M. McQueen, Y. S. Lee, C. Payen and D. G. Nocera, *Chem. Commun.*, 2012, **48**, 64–66.
5 Y. She, Y. Wang, S. Li, T. Wang and H. Lu, *Nano Res.*, 2022, **16**, 3552–3557.
6 M. B. Sanders, J. W. Krizan and R. J. Cava, *J. Mater. Chem. C*, 2016, **4**, 541–550.
7 A. Li, Y. Wang, H. Tian, A. Yalikun, Y. Journaux, M. Luo and H. Lu, *Chin. Chem. Lett.*, 2023, **35**, 108780.
8 F. H. Aidoudi, D. W. Aldous, R. J. Goff, A. M. Z. Slawin, J. P. Attfield, R. E. Morris and P. Lightfoot, *Nat. Chem.*, 2011, **3**, 801–806.
9 R. S. Dissanayaka Mudiyanselage, T. Klimczuk, D. Ni, R. J. Cava and W. Xie, *Inorg. Chem.*, 2022, **61**, 18010–18018.
10 A. F. Albuquerque, D. Schwandt, B. Hetényi, S. Capponi, M. Mambrini and A. M. Läuchli, *Phys. Rev. B: Condens. Matter Mater. Phys.*, 2011, **84**, 024406.
11 N. Shannon, T. Momoi and P. Sindzingre, *Phys. Rev. Lett.*, 2006, **96**, 027213.
12 M. Ashtar, Y. Bai, L. Xu, Z. Wan, Z. Wei, Y. Liu, M. A. Marwat and Z. Tian, *Inorg. Chem.*, 2021, **60**, 3626–3634.
13 J. T. Chalker, P. C. W. Holdsworth and E. F. Shender, *Phys. Rev. Lett.*, 1992, **68**, 855–858.
14 R. Moessner and S. L. Sondhi, *Phys. Rev. Lett.*, 2001, **86**, 1881–1884.
15 J. E. Greedan, *J. Mater. Chem.*, 2001, **11**, 37–53.
16 W. Liu, Z. Zhang, J. Ji, Y. Liu, J. Li, X. Wang, H. Lei, G. Chen and Q. Zhang, *Chin. Phys. Lett.*, 2018, **35**, 117501.
17 Y. Gao, L. Xu, Z. Tian and S. Yuan, *J. Alloys Compd.*, 2018, **745**, 396–400.
18 F. Song, A. Liu, Q. Chen, J. Zhou, J. Li, W. Tong, S. Wang, Y. Wang, H. Lu, S. Yuan, H. Guo and Z. Tian, *Inorg. Chem.*, 2024, **63**, 5831–5841.
19 Y. Saito, T. Minamidate, A. Kawamoto, N. Matsunaga and K. Nomura, *Phys. Rev. B*, 2018, **98**, 205141.
20 J. Alicea, A. V. Chubukov and O. A. Starykh, *Phys. Rev. Lett.*, 2009, **102**, 137201.
21 J. Sheng, L. Wang, A. Candini, W. Jiang, L. Huang, B. Xi, J. Zhao, H. Ge, N. Zhao, Y. Fu, J. Ren, J. Yang, P. Miao, X. Tong, D. Yu, S. Wang, Q. Liu, M. Kofu, R. Mole, G. Biasiol, D. Yu, I. A. Zaliznyak, J.-W. Mei and L. Wu, *Proc. Natl. Acad. Sci. U. S. A.*, 2022, **119**, e2211193119.
22 M. Liu, H. Zhang, X. Huang, C. Ma, S. Dong and J. Liu, *Inorg. Chem.*, 2016, **55**, 2709–2716.
23 S. Nakatsuji, Y. Nambu, H. Tonomura, O. Sakai, S. Jonas, C. Broholm, H. Tsunetsugu, Y. Qiu and Y. Maeno, *Science*, 2005, **309**, 1697–1700.
24 Y. Shirata, H. Tanaka, T. Ono, A. Matsuo, K. Kindo and H. Nakano, *J. Phys. Soc. Jpn.*, 2011, **80**, 093702.
25 S. Das, S. Hossain, A. Dey, S. Biswas, J.-P. Sutter and V. Chandrasekhar, *Inorg. Chem.*, 2014, **53**, 5020–5028.
26 J. Goura, J. P. S. Walsh, F. Tuna and V. Chandrasekhar, *Inorg. Chem.*, 2014, **53**, 3385–3391.
27 Y. Li, H. Liao, Z. Zhang, S. Li, F. Jin, L. Ling, L. Zhang, Y. Zou, L. Pi, Z. Yang, J. Wang, Z. Wu and Q. Zhang, *Sci. Rep.*, 2015, **5**, 16419.
28 M. Ashtar, M. A. Marwat, Y. X. Gao, Z. T. Zhang, L. Pi, S. L. Yuan and Z. M. Tian, *J. Mater. Chem. C*, 2019, **7**, 10073–10081.
29 M. Ashtar, Y. X. Gao, C. L. Wang, Y. Qiu, W. Tong, Y. M. Zou, X. W. Zhang, M. A. Marwat, S. L. Yuan and Z. M. Tian, *J. Alloys Compd.*, 2019, **802**, 146–151.
30 J. Xing, L. D. Sanjeewa, J. Kim, G. R. Stewart, M. H. Du, F. A. Reboredo, R. Custelcean and A. S. Sefat, *ACS Mater. Lett.*, 2020, **2**, 71–75.
31 Z. Ma, J. Wang, Z. Dong, J. Zhang, S. Li, S. Zheng, Y. Yu, W. Wang, L. Che, K. Ran, S. Bao, Z. Cai, P. Čermák, A. Schneidewind, S. Yano, J. S. Gardner, X. Lu, S. Yu, J. Liu, S. Li, J. Li and J. Wen, *Phys. Rev. Lett.*, 2018, **120**, 087201.
32 Z. Hu, Z. Ma, Y.-D. Liao, H. Li, C. Ma, Y. Cui, Y. Shangguan, Z. Huang, Y. Qi, W. Li, Z. Y. Meng, J. Wen and W. Yu, *Nat. Commun.*, 2020, **11**, 5631.
33 U. K. Voma, S. Bhattacharya, E. Kermarrec, J. Alam, Y. M. Jana, B. Sana, P. Khuntia, S. K. Panda and B. Koteswararao, *Phys. Rev. B*, 2021, **104**, 144411.
34 S.-Y. Zhang, W.-B. Guo and Z.-Z. He, *Dalton Trans.*, 2019, **48**, 65–71.
35 S. Guo, R. Zhong, K. Górnicka, T. Klimczuk and R. J. Cava, *Chem. Mater.*, 2020, **32**, 10670–10677.
36 M. Cui, N. Wang, S. Chen, X. Huang and Z. He, *J. Alloys Compd.*, 2019, **785**, 1009–1014.
37 H. Liu, Y. Wang, Y. Zhou, S. Li, Y. Dou, T. Wang and H. Lu, *Inorg. Chem.*, 2022, **61**, 17838–17847.
38 X. Huang, Z. Zhao, M. Zhang and Z. He, *CrystEngComm*, 2021, **23**, 3126–3132.
39 A. Yalikun, Y. Wang, Y. Lv, Y. Dou, H.-J. Koo, J. Cao, W. Qi, K. Huang, M.-H. Whangbo, Z. Ouyang and H. Lu, *Inorg. Chem.*, 2024, **63**, 14354–14365.
40 Z. He and W. Cheng, *Solid State Commun.*, 2009, **149**, 236–238.
41 M. B. Sanders, F. A. Cevallos and R. J. Cava, *Mater. Res. Express*, 2017, **4**, 036102.
42 Y. Wang, S. Li, Y. Dou, H. Li and H. Lu, *Dalton Trans.*, 2023, **52**, 13555–13564.
43 H. Li, S. Li, Y. Wang, Y. Dou and H. Lu, *J. Solid State Chem.*, 2025, **341**, 125052.
44 C. Tao and R. Li, *Chem. – Eur. J.*, 2020, **26**, 3709–3712.
45 X. Chen, R. Bian, W. Xiao and X. Song, *Dalton Trans.*, 2022, **51**, 9454–9466.
46 X. Chen, X. Yuan, W. Xiao and X. Song, *RSC Adv.*, 2024, **14**, 6270–6284.
47 G. M. Sheldrick, *Acta Crystallogr.*, 2015, **71**, 3–8.
48 P. P. Sahoo, E. Gaudin, J. Darriet and T. N. Guru Row, *Mater. Res. Bull.*, 2009, **44**, 812–816.
49 H. Xie, X. Chang, W. Yang, Y. Jiang and Y. Zhao, *Synth. React. Inorg. Met.-Org. Chem.*, 2016, **46**, 1090–1094.

50 J. Rodríguez-Carvaja, *Phys. B*, 1993, **192**, 55–69.
51 G. A. Bain and J. F. Berry, *J. Chem. Educ.*, 2008, **85**, 532–536.
52 L. Vijayalakshmi, K. Naveen Kumar and J. D. Baek, *J. Mater. Sci.:Mater. Electron.*, 2022, **33**, 11938–11945.
53 L. Vijayalakshmi, K. Naveen Kumar, G. Srinivas, P. Hwang and J. Choi, *Optik*, 2021, **227**, 166025.
54 R. Liu, H. Wu, H. Yu, Z. Hu, J. Wang and Y. Wu, *Chem. Mater.*, 2021, **33**, 4240–4246.
55 A. B. Kuznetsov, K. A. Kokh, N. Sagatov, P. N. Gavryushkin, M. S. Molokeev, V. A. Svetlichnyi, I. N. Lapin, N. G. Kononova, V. S. Shevchenko, A. Bolatov, B. Uralbekov, A. A. Goreiavcheva and A. E. Kokh, *Inorg. Chem.*, 2022, **61**, 7497–9505.
56 Y. Chen, P. Gong, R. Guo, F. Fan, J. Shen, G. Zhang and H. Tu, *Inorg. Chem.*, 2023, **62**, 15584–15592.
57 P. Chen, M. M. Murshed and T. M. Gesing, *J. Mater. Sci.*, 2020, **56**, 3639–3652.
58 Y. Li, W. Liu, Y. Li, X. Li, Y. Gao, Z. Tian and M. Wang, *Solid State Sci.*, 2025, **169**, 108095.
59 D. Gelija, H.-a. Kim and W. J. Chung, *Opt. Mater.*, 2025, **167**, 117251.
60 N. Kawano, K. Shinozaki, D. Nakauchi, H. Kimura, G. Okada and T. Yanagida, *Mater. Res. Bull.*, 2023, **158**, 112081.
61 A. D. Sontakke and K. Annapurna, *Mater. Chem. Phys.*, 2013, **137**, 916–921.
62 M. A. Marzouk, F. H. ElBatal, Y. M. Hamdy and H. A. ElBatal, *Appl. Phys. A*, 2023, **129**, 505.
63 N. Yaduvanshi, C. Basavapoornima, A. S. Alqarni, U. K. Kagola, T. Uthayakumar, A. Madhu and N. Srinatha, *Opt. Mater.*, 2024, **151**, 115359.
64 Q. Chen, M. Zhang, Q. Ma and Q. Wang, *J. Non-Cryst. Solids*, 2019, **507**, 46–55.
65 J. Tauc, R. Grigorovici and A. Vancu, *Phys. Status Solidi B*, 1966, **15**, 627–637.
66 X. Xu, C. L. Hu, B. X. Li and J. G. Mao, *Chem. – Eur. J.*, 2016, **22**, 1750–1759.
67 Z. Ma, S. Zheng, Y. Chen, R. Xu, Z.-Y. Dong, J. Wang, H. Du, J. P. Embs, S. Li, Y. Li, Y. Zhang, M. Liu, R. Zhong, J.-M. Liu and J. Wen, *Phys. Rev. B*, 2024, **109**, 165143.
68 Y. Lv, Y. Wang, Y. Dou, A. Li, J. Tang, O. S. Volkova, A. N. Vasiliev and H. Lu, *Cryst. Growth Des.*, 2025, **25**, 2446–2455.
69 M. Ashtar, J. Guo, Z. Wan, Y. Wang, G. Gong, Y. Liu, Y. Su and Z. Tian, *Inorg. Chem.*, 2020, **59**, 5368–5376.
70 S. Guo, T. Kong, W. Xie, L. Nguyen, K. Stolze, F. A. Cevallos and R. J. Cava, *Inorg. Chem.*, 2019, **58**, 3308–3315.
71 P. Mukherjee, A. C. Sackville Hamilton, H. F. J. Glass and S. E. Dutton, *J. Phys.: Condens. Matter*, 2017, **29**, 405808.
72 E. C. Koskelo, C. Liu, P. Mukherjee, N. D. Kelly and S. E. Dutton, *Chem. Mater.*, 2022, **34**, 3440–3450.
73 Q. Zeng, H. Ge, M. Wu, S. Ruan, T. Li, Z. Wang, J. Li, L. Ling, W. Tong, S. Huang, A. Liu, J. Zhou, Z. Xia, J. Sheng, L. Wu and Z. Tian, *Chem. Mater.*, 2024, **36**, 2867–2879.
74 (*a*) CCDC 2466013: Experimental Crystal Structure Determination, 2026, DOI: 10.5517/ccdc.csd.cc2ns2tc; (*b*) CCDC 2466014: Experimental Crystal Structure Determination, 2026, DOI: 10.5517/ccdc.csd.cc2ns2vd; (*c*) CCDC 2466015: Experimental Crystal Structure Determination, 2026, DOI: 10.5517/ccdc.csd.cc2ns2wf; (*d*) CCDC 2466016: Experimental Crystal Structure Determination, 2026, DOI: 10.5517/ccdc.csd.cc2ns2xg.